ADVANCED ENGINEERING MATERIALS
www.aem-journal.com

Inkjet-Printed Ag/a-TiO_2/Ag Neuromorphic Nanodevice Based on Functionalized Ink

Barbara Salonikidou, Adnan Mehonic, Yasunori Takeda, Shizuo Tokito, Jonathan England, and Radu A. Sporea*

This study aims to contribute to the burgeoning field of brain-inspired computing by expanding it beyond conventional fabrication methods. Herein, the obstacles toward the effective inkjet printing process are encountered and the electrical characteristics are explored, providing new insights into the reliability aspects of fully printed Ag/a-TiO_2/Ag electronic synapses. The versatility of the approach is further enhanced by the highly stable in-house-developed a-TiO_2 ink, exhibiting optimal shelf life of five months and repeatable jetting, producing layers with nanoscale thickness resolution. Most importantly, device electrical characterization reveals synaptic dynamics, leading to activity-dependent conductance state retention and adaptation characteristics, implying inherent learning capabilities. The synaptic dynamics are attained by solely adjusting the duty cycle of the applied pulsed voltage trigger, while keeping amplitude and polarity fixed, a method readily compatible with realistic applications. Furthermore, *I–V* analysis demonstrates a dynamic range dependence on a-TiO_2 layer thickness and conduction mechanism that is akin to the conventionally developed electronic TiO_2 synapses. The developed devices provide a time- and cost-effective ecologically benign alternative toward biomimetic signal processing for future flexible neural networks.

1. Introduction

The notion of electronics mimicking biological working principles has existed for a long time.[1,2] Distinct from the widely used von Neumann computational architecture,[3] bioinspired computing enables processing which is comparable with that performed by the brain during memorization and learning.[4,5] The past two decades have seen a growing trend toward two-terminal resistive switching (RS) devices, named electronic synapses, owing to their simple structure and resistance-state transitions that obey biosynaptic processing principles.[6,7] Vital for dynamic adaptation and event-based learning,[4] such biomimetic properties make them competent to operate both as computational and as memorization nodes in neuromorphic electronics.[3,8–10]

In biological neuronal circuits, memorization and learning are inherently controlled through communication between neurons, via small junctions, named synapses. The transfer of information occurs through action potentials, which are electrical impulses, caused by the movement of ions and signaling molecules (neurotransmitters) across the cell membrane, inducing brief changes in conductance.[11,12] The synaptic strength or efficacy w between adjacent neurons is altered according to the timing and history of past events, a phenomenon that is called synaptic plasticity. Specifically, synaptic plasticity is classified into short term when the retention range is milliseconds–minutes and long term when the retention is extended to hours or years. Synaptic efficacy is bidirectional, as it can be enhanced or weakened, depending on trigger timing and intensity, leading to event-based changes in synaptic plasticity.[13] While under tetanic stimulation (application of high-frequency or prolonged duration trigger) and/or increased number of iterations, long-term potentiation (LTP) is prompted; when low-frequency stimuli is followed, depression is evoked that is expressed through w weakening and associated with the forgetting effect.[14–17] Short-term potentiation (STP) is widely studied through paired-pulse facilitation (PPF), during which a pair of action potentials is applied at neuronal presynaptic axon terminals, with the second impulse inducing the stronger release of neurotransmitters and w enhancement that is expressed through increased action potential at postsynaptic terminals.[13,18] The postsynaptic increase

B. Salonikidou, J. England, R. A. Sporea
Advanced Technology Institute (ATI)
University of Surrey
Stagg Hill 388, Guildford GU2 7XH, UK
E-mail: v.salonikidou@surrey.ac.uk

B. Salonikidou
Materials Science & Metallurgy
University of Cambridge
27 Charles Babbage Road, Cambridge CB3 0FS, UK

A. Mehonic
Department of Electronic & Electrical Engineering
UCL
Torrington Place, London WC1E 7JE, UK

Y. Takeda, S. Tokito
Research Center for Organic Electronics (ROEL)
Yamagata University
4-3-16 Jonan, Yonezawa, Yamagata 992-8510, Japan

The ORCID identification number(s) for the author(s) of this article can be found under https://doi.org/10.1002/adem.202200439.

DOI: 10.1002/adem.202200439

occurs in a stepwise fashion, signifying a temporal summation of amplitude that is conditional to the time interval between the applied pair of impulses.[11,19] This second-order phenomenon is governed by Ca^{2+} residual in the neuronal membrane, adjusted by the timing characteristics of stimuli.[20,21] Even though STP duration is brief, it is vital for temporal processing purposes.[22,23] The conditions under which transitions from STP to LTP occur constitute the basis of activity-based learning.[15,16]

The two-terminal electronic synapses are composed of an active material, in principle, an insulator or a wide-gap semiconductor, positioned between the bottom and top electrode. These minimal devices are qualified for the realization of multiple conductance states, altered according to the timing and history of applied voltage triggers.[24–26] The conductance state modulation, analogous to biosynaptic strength, is expected to occur following plasticity working principles introduced earlier. For the interpretation of RS during high- and low-resistance states, the background conduction mechanism is widely investigated through *I–V* sweeps and is classified into two main categories: the electrode limited and the bulk limited. Electrode-limited conduction is associated with the interfacial properties between active layer and electrode and includes Schottky emission, Fowler–Nordheim tunneling, thermionic emission, and direct tunneling. Bulk-limited conduction is governed by the properties of the active layer itself and consists of: ohmic conduction, grain boundary-limited conduction, space–charge-limited conduction (SCLC), ionic, hopping, and Poole–Frenkel conduction. The driving mechanisms with their subcategories are extensively covered in several reviews.[27,28] Reports have revealed that amorphous TiO_2 (a-TiO_2) possesses electronic properties and transport properties that are similar to its bulk crystalline phases,[29,30] a property that opens a path toward a cheaper and abundant alternative to realize analog RS cells.[31,32] In both a-TiO_2 and c-TiO_2-based devices, the choice of the electrode material affects in a similar manner the charge transport during voltage application. When inert electrodes, such as Pt, are used, SCLC principally governs the RS at low voltages, while Schottky emission takes place at high voltages, in both c-TiO_2[33] and a-TiO_2.[34] When active (electrochemically) electrodes (e.g., Ag, Al) are implemented, ohmic conduction is shown to affect the switching at low voltages and a bulk, or electrode, limited at higher electric fields, depending on various factors, including thickness and deposition process.[35–37] A key challenge today of such devices to be utilized as computational nodes in neuromorphic applications includes the effective control of gradual current increase with each voltage trigger, following PPF principles,[38] along with STP-to-LTP transitions, ideally modulated through trigger-timing characteristics that will be easily implemented in realistic applications.[39]

Considering a-TiO_2 capability to be synthesized through a wide range of methods, including the most versatile ones of solvothermal and sol–gel, it becomes compatible with solution-processed techniques characterized by low complexity. As an alternative to traditional methods of radio frequency (RF) reactive sputtering[40,41] and plasma-enhanced ALD,[42] inkjet printing (IJP) constitutes an ecofriendly and scalable technique, that enables fabrication of flexible and large-area neural networks with production scalability at minimum fabrication costs.[43,44] However, the existing reports on synthesis of functional inks that can be reliably jetted after long storage periods while sustaining their electronic properties are absent and need to be addressed. Moreover, the formation of cracks and fissures in TiO_2 solution-processed layers further hinders the progress of such devices.[45–48] The concurrent maturing of IJP technology and increasing interest in two-terminal RS devices make it a timely opportunity to investigate the dynamic properties of these artificial synapses and overcome reliability obstacles toward fully printed neuromorphic devices.

In this work, two functional inks consisting of titanium isopropoxide (TTIP): stabilizing agents (acetic acid and acetylacetone) 1:4 and 1:8 molar ratios are prepared and characterized. The jettability properties, nanoparticle size, and chemical structure of the derived crack-free printed nanolayers are presented. The dynamic properties of the developed fully printed Ag/a-TiO_2/Ag electronic synapses are studied through voltage pulses. The synaptic processing and retention capabilities are investigated in a manner that is directly applicable to bioinspired processing (e.g., biomimetic sensing for electronic skin), by modulating the trigger duty cycle while voltage amplitude was kept constant. The findings demonstrated STP and LTP attributes that were conditional to trigger intensity and duration, strikingly similar to their biological counterparts. Furthermore, the relation of a-TiO_2 layer thickness to RS properties is discussed and *I–V* measurements are conducted to extract information about the conduction mechanism.

2. Results and Discussion

2.1. Characterization of Functional a-TiO_2 Inks and Inkjet Printing of Ag/a-TiO_2/Ag Electronic Synapses

For the development of a-TiO_2 nanolayers, two custom-made inks were synthesized and optimized for optimal jettability and shelf life. When developing custom functional inks, the rheological requirements of the inkjet printer nozzle, as well as the surface properties of the substrate or target layer, should be considered. The critical factors that determine jetting reliability, that is, the consistent ejection of stable droplets, can be combined in the physical constant Z.

$$Z = \frac{(d \times \rho \times \gamma)^{1/2}}{\eta} \tag{1}$$

where d is the diameter of the printer nozzle (in the present case of Fujifilm Dimatix DMP 2850 series was 21.5 μm), ρ is ink density (kg m^{-3}), γ is surface tension (mN m^{-1}), and η is ink viscosity (mPa s). The parameters must be adjusted so that the value of Z lies between the range of 1 and 10 for reliable jetting, without forming satellite droplets or demanding high driving voltage for droplet ejection that eventually damages the cartridge head.[49,50] Generally, to secure compatibility with Dimatix cartridge head, inks should contain particles with sizes below 200 nm and viscosities between 5 and 40 mPa s to prevent any clogging effect.[51] A stable ink, without sedimentation, eliminates the appearance of aggregations that will potentially harm the cartridge and decrease ink shelf life.

In this work, the active ink synthesis relied on Ti isopropoxide (TTIP) hydrolysis and condensation reactions. Acetic acid (AcOH) and acetylacetone (ACAC) were implemented as a

stabilizing agent mixture (S.A). Two active inks were prepared with molar ratios of TTIP:SA of 1:8 (ink_1) and 1:4 (ink_2) (detailed information on the synthesis can be found in the Experimental Section). The viscosity and surface tension of ink_1 (ink_2) were defined experimentally and found to be ≈8 mPa s (9 mPa s) and 31 mN m^{-1} (30 mN m^{-1}), that resulted in Z number of 3.3–3.5, which was within the acceptable range for efficient jetting.[49] The pH for both cases was around 4 (±0.3), that was optimal for continuous jetting, without causing any damage to the cartridge and nozzles.

The chemical structure of the inks was characterized through X-Ray photoelectron spectroscopy (XPS). The binding energies (BE) of Ti (**Figure 1a)** and O (Figure 1b) in both inks demonstrated a characteristic separation of 72.4 eV between the $Ti2p_{3/2}$ and O1s peaks, in agreement with TiO_2 reported values that range between 72.9 and 71.2 eV.[52] Ink_1 (black line) presented BE peaks of $Ti2p_{3/2}$ located at 458.88 eV, $Ti2p_{1/2}$ at 464.48 eV, and O1s at 531.28 eV. The detected peaks were all shifted by +0.4 eV relative to ink_2 (458.48, 464.08, and 530.88 eV, respectively. Values shown with red line), implying direct control through synthesis. The BEs of O1s were slightly higher than 530 eV, attributed to Ti—O bonds; thus, the slight shift in the present case most possibly was related to defects (e.g., oxygen-deficient regions) and carbon bonds that have also been previously reported in solution-processed a-TiO_2 and c-TiO_2 layers.[53–55] The XPS survey spectrum with the concentration of additional elements can be found in Supplementary Information (Figure S1 and Table S1, Supporting Information, respectively).

Dynamic light scattering (DLS) measurements were performed to investigate the nanoparticle size and distribution of both inks. The results presented polydisperse size distribution, with nanoparticles in the range of 20–28 nm for ink_1 and relatively narrow distribution with nanoparticles between 30 and 40 nm for ink_2 (Figure 1c). Ink_1 characterization repeated after a period of five-month storage and showed about fivefold size increase due to agglomerations formed over time (Figure 1c, blue

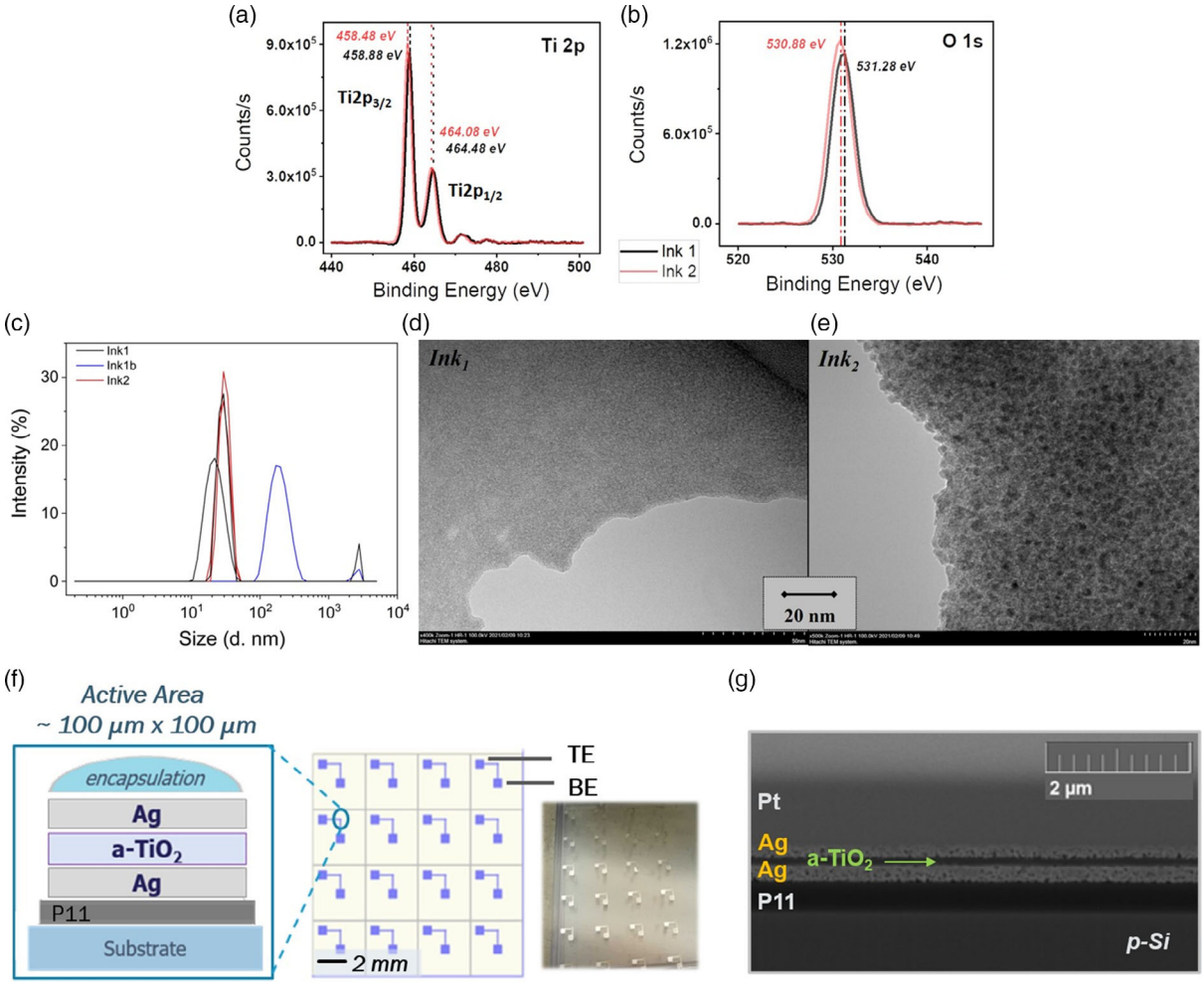

Figure 1. Chemical and nanoparticle characterization of the synthesized a-TiO_2 inks. High-resolution XPS spectra of a) Ti2p doublet and b) O1s of inks (ink_1 in black and ink_2 in red), both presenting TiO_2 characteristic binding energies. c) DLS measurements of ink_1 (black), ink_2 (red) and ink_1 5 months after synthesis (Ink1b, blue) showing ink stability with nanoparticle size within the acceptable range, over this timescale. Top-down TEM images of Ink_1 d) and Ink_2 e) (see Methodology Chapter). f) Cross-sectional illustration of the printed a-TiO_2 electronic synapses on the designed array (left) and top-down optical image of the printed array (right) g) cross-sectional scanning electron microscope (SEM) image of the printed layers on *p*-type c-Si (see Methodology Section).

line). The ink exhibited undisrupted jetting, retaining its properties (Figure S2, Supporting Information, depicts ink droplets' ejection, as shown in printer stroboscopic camera, five months after synthesis). Considering that ink consistency in custom-made inks is a key challenge,[51] the present results constitutes a considerable achievement. Even though DLS showed an increase in particle size, the measured values corresponded to particle clusters that were formed over time but easily broke during jetting, due to nozzle stimulation by tickle pulses (periodical movement of nozzle meniscus that slightly agitates the ink close to the orifice).[56] To get a better insight into particle morphology, transmission electron microscopy (TEM) was used as a supplementary technique for particle visualization. In Figure 1d,e, TEM images depict the granular and polydisperse nature of the developed inks. Ink_1 consisted of nanoparticles with sizes around and below 2 nm (Figure 1d), while ink_2 contained nanoparticles ranging between 2 and 6 nm (Figure 1e). The discrepancy between DLS and TEM measurements exists due to DLS inability to distinguish particle aggregations. In both cases, ink_2 is shown to have about two times larger nanoparticle size compared with ink_1, that shows a direct correlation between TTIP:SA ratio and particle size.

The IJP process followed successful ink preparation. IJP occurred under ambient conditions in a drop-on-demand mode, which enables development of layers through sequential deposition of ink droplets of pL volume.[51,57] The device fabrication followed a sequential process of deposition and thermal treatment, from bottom to top, as shown in the cross-sectional illustration in Figure 1f (see Experimental Section for further information related to fabrication). Figure 1f also depicts the array design and the corresponding top-down optical image of the printed array. The shape and thickness of the layers were controlled through positioning of droplets and drop space (distance between two sequential drops, in μm). The drop space was set at 20–22 μm for both Ag and TiO_2 for the formation of continuous, uniform, and well-defined stacked nanolayers, as shown in SEM image (Figure 1g). The bottom and top electrodes were around 220 nm (2D layer profile shown in Figure S4, Supporting Information) and 150 nm thick, respectively. The active layer was treated at low temperature at around 90 °C for 10 min, that was sufficient for solvent evaporation, as no thickness change was observed after this duration (Figure S3, Supporting Information) and the electrical properties followed during electrical characterization were consistent. For the a-TiO_2 active layers, it was deduced that there was an optimal range, between 80 nm and 350 nm, for the development of functional devices. Specifically, a-TiO_2 layers below 80 nm resulted in uncovered areas (see the SEM picture in Figure S5a, Supporting Information) and consequently interconnection between electrodes and device failure, whereas layers over 350 nm thickness increased the probability of crack (microscopy picture based on our previous report presented in Figure S5b, Supporting Information)[58] formation and also raised considerably the power requirements for switching (>30 V). With ink_1, a single IJP scan was used for the formation of thin a-TiO_2 layers, in the range of 80 nm, without any surface pretreatment. While for thicker layers, ranging from 250 to 400 nm, 3–5 IJP scans were required. Ink_2 generated thicker (by 30 nm $scan^{-1}$) printed layers, that is in direct relation to TTIP:SA and derived particle size.

Conclusively, in this work, the deleterious crack formation in a-TiO_2 printed layers was prevented by implementing synthesis of low cost and complexity. The small nanoparticle size of the functionalized inks, controlled through the TTIP:SA molar ratio, decreased the development of cracks and fissures. Furthermore, in contrast to our previous report that demonstrated the prevalence of cracks at layer thickness above 120 nm,[58] here, the incorporation of ACAC decreased the solution evaporation rate and prevented the pressure gradient in the printed layer that previously resulted in different shrinkage rates between the inner and outer layer regions.[59] Through TTIP:SA, the effective layer thickness control was attained, with 80 (ink_1) and 120 nm (ink_2) resolution. The electrical properties of the derived Ag/a-TiO_2/Ag electronic synapses are presented and discussed in the following sections.

2.2. Electrical Characterization

2.2.1. Paired-Pulse Facilitation (PPF) and Timing-Dependent Plasticity Controlled through Voltage Pulse Train Duty Cycle α

In this work, we investigated the synaptic attributes of PPF and timing-dependent plasticity in printed Ag/TiO_2/Ag electronic synapses, through sequential voltage pulses (V_{in}) that applied across device terminals, and the output current (I_{out}) was measured. The plasticity properties were explored by solely modulating the duty cycle α, defined as

$$\alpha = \frac{\text{Pulse duration}}{\text{Period } T} \times 100(\%) \tag{2}$$

On Ag/a-$TiO_{2(250\,nm)}$/Ag device (device 1), 240 voltage pulses with V_{in} amplitude = 1 V, frequency f = 4 Hz, and duty cycle α = 20% (pulse duration = 50 ms and period T = 250 ms, green lines in **Figure 2**a) were sequentially applied. I_{out} during the initial 5 s and during the whole measurement period of 60 s are illustrated in Figure 2a,b, respectively. I_{out} presented a stepwise increase under voltage pulses, that was linear during the initial 5 s (Figure 2a), implying analog RS capabilities, whereas the rate of current increase lessened after around 15 s (Figure 2b). To approximately quantify the temporal dynamics, the synaptic modification Δw (%) was also investigated.

$$\Delta w = \frac{I_{out2} - I_{out1}}{I_{out1}} \times 100(\%) \tag{3}$$

where I_{out1} and I_{out2} are the currents measured before and after V_{in} application, respectively. The derived Δw versus the number of applied pulses are presented in Figure 2c. Δw demonstrated initially a steep increase in current, while attenuation was observed after around 50 pulses, behavior that is in alignment with plasticity-induced self-adaptation found in biological synapses.[4,60,61] Self-adaptation aids in high-performance functionalities, such as event-based learning and perception, essential for the flourishing of neuromorphic networks.[39,62]

In Figure 2d the effect of α on the I_{out} increase is demonstrated. In this experiment, a printed device with 200 nm

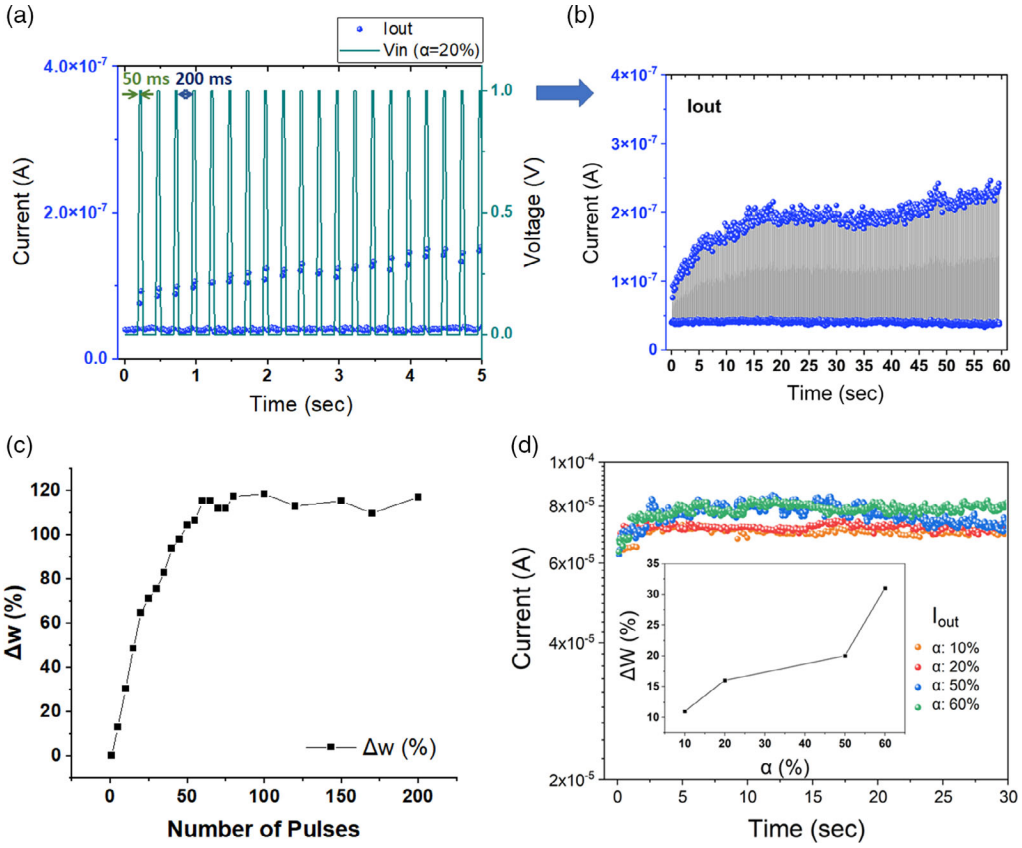

Figure 2. Paired-pulse Facilitation (PPF) with duty cycle α dependence on current growth. a) Current-time (I–t) plot presents the applied pulsed voltage train (V_{in}: 1 V, 4 Hz, α: 20%, green lines) on device 1 (Ag/$TiO_{2(250\,nm)}$/Ag), and the corresponding stepwise increase of I_{out} (blue datapoints), during the first 5 s and b) during 60 s) Δw (%) versus the number of applied pulses as derived from b), showing a steep increase in I_{out}, that is flattened after around 50 pulses, implying a form of adaptation under repeated stimuli. d) I–t plot illustrates the current response under increasing α (10%, 20%, 50% and 60%) during 30 s of V_{in} (1 V, 4 Hz), occurred with 60 s intervals on device 2 (Ag/$TiO_{2(200\,nm)}$/Ag). In the inset, the Δw (%) versus the number of applied pulses are illustrated, showing a potentiation dependence to α (%).

a-TiO_2 thickness (device 2) was tested under four subsequent V_{in} with increasing α. The amplitude and frequency were kept fixed at 1 V and 4 Hz, respectively, while α was altered sequentially as follows: 10–20–50–60%. As expected, the average measured I_{out} in this case was increased by ≈2 orders of magnitude, owing to the thinner (by ≈50 nm) active layer. The results showed a Δw of ≈12% (17%) under low α 10% (20%), while for 50 and 60%, duty cycle Δw rose to ≈20% and 33%, respectively (Figure 2d inset). For $\alpha = 60\%$, a sustainable higher current growth (by ≈10 μA) was observed, as illustrated in Figure 2d. Overall, independent of the active layer thickness, current growth exhibited nonlinear characteristics, with an initial buildup followed by attenuation. The stepwise current increase was also observed when double-pulsed trigger of 2 and 4 V was applied, also showing continuous conductance modulation that is amplitude dependent and not affected by voltage alterations (Figure S6, Supporting Information). This type of sequential and variability-tolerant processing can also be achieved when a set of high- and low-duty cycle pulses are applied successionally, as demonstrated in this work (section: 'Event-based continuous and repeatable conductance state modulation').

3. Internal Dynamics

To interpret the internal dynamics responsible for the synaptic properties of both device 1 and device 2, electrical characterizations under low read voltage pulses, $V_{read} = 80$ mV with $\alpha = 80\%$ (**Figure 3**a) were conducted 20 s after V_{in} (1 V, $\alpha = 20\%$, overall duration 200 s) and used for conductance state acquisition. The amplitude was set at low level to not affect the conductance even when small intervals were used. The current response, I_{read}, was characterized by a power law relaxation, as illustrated in Figure 3b, that is akin to transient Ca^{2+} decay at synaptic membrane after stimulation.[18] In biological synapses, Ca^{2+} concentration plays a key role in shaping timing-dependent plasticity, owing to the synaptic strength control it provides, by increasing (decreasing) the probability of strengthening (weakening) after a follow-up impulse arrives in a short (long) time window.[63] Likewise in electronic synapses, the course of decay sets the timeframe under which a temporal summation can occur and thus it's vital for event-based processing and encoding specific to neuronal circuits.[11]

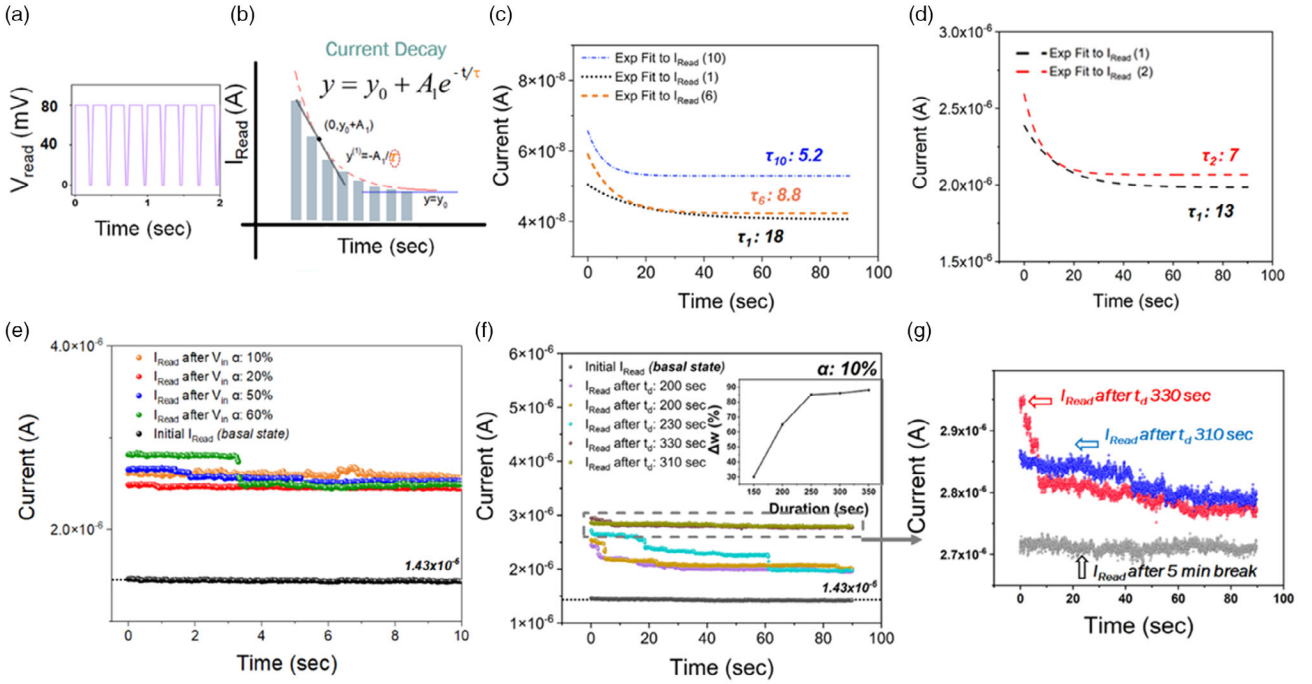

Figure 3. Relaxation dynamics of printed Ag/a-TiO_2/Ag electronic synapses a) V_{read} (80 mV, α: 80%, f: 4 Hz) applied after triggering to read the device conductance state b) Equation used for the exponential fit in current decay and time constant τ calculation. c) V_{read} applied after V_{in} (1 V, α: 20%, f: 4 Hz, duration: 200 s) and the corresponding fitted (dashed) with their time constants τ after 1st, 6th and 10th repetition on device 1 are shown. d) The corresponding fitted I_{read} (dashed) and their time constants τ after 1st and 2nd repetition on device 2. e) I_{read} after V_{in} of α: 10, 20, 50 and 60% with reference to the basal state (black). f) I_{read} after V_{in} of α: 10% with durations (t_d) ranging from 200–330 s and the corresponding Δw versus trigger duration (inset), showing the effect of adaptation after around 250 s. g) I_{read} after V_{in} with α: 10% and duration 310 sec (blue) and 330 sec (red) with reference to the measurement results after 5 min break (grey).

The impact of the number of iterations on I_{read} was explored through the characteristic time constant decay τ, expressed through the exponential function.

$$y = y_0 + A_1 \times e^{-t/\tau} \tag{4}$$

where τ is the relaxation time constant, t is the time following V_{read}, and A_1 and y_0 are positive fitting constants. The corresponding fitted I_{read} is illustrated in Figure 3c (device 1) and Figure 3d (device 2). In both cases, I_{read} was augmented and τ was decreased after each iteration, implying easier transition to higher-conductance states with trigger repetition. However, device 1 exhibited τ drop of ≈50% after five V_{in} repetitions (from 18 to 8.8), while device 2 showed the same percentage of reduction after only two sweeps (from 13 to 7), indicating that the thinner active layer prompts faster rate of conductance increase. The retention of device 2 after stimulation with different duty cycles was also tested. The relaxation dynamics are illustrated in Figure 3e, showing an increased I_{read} (≈$2.8\,10^{-6}$ A) retained for around 3 s and then relaxed to a low level (around 2.5×10^{-6} A), when V_{in} of 60% duty cycle preceded V_{read}. However, when V_{in} was 50, 20, or 10%, I_{read} was kept closer to the low level. The findings imply that triggers of α up to 60% and duration of 200 s induce STP with retention conditional to the length of duty cycle.

In addition, current augmentation under low α was feasible when triggering was prolonged. In Figure 3f, I_{read} was measured after sequential V_{in} cycles of different overall durations, ranging from 200 to 330 s. The results displayed a rise in conductance corresponding to the trigger duration, with 230 s inducing longer STP that relaxed to the low conductance level after 60 s (green in Figure 3f). However, 310 and 330 s trigger durations expanded the retention to over 90 s. The reading measurements repeated after 5 min of voltage break and showed a slight current decrease (≈0.08 μA), depicted in Figure 3g. However, I_{read} was well above the basal state indicating LTP. The basal state here corresponds to the conductance state before any stimulation occurs, that was measured on a weekly basis for 1 month and found to be around 1.4×10^{-6} A, shown in black in Figure 3e,f. The inset of Figure 3g presents Δw versus trigger duration and demonstrates attenuation after V_{in} of around 250 s, suggesting that learning functionalities are attainable with mild stimulation when its duration is prolonged.

The characterization of the printed electronic synapses demonstrates a current modulation through the voltage duty cycle and a rate of processing that can be controlled though a-TiO_2 layer thickness, which is an easily adjustable process through IJP. τ can be further reduced as observed in our previously developed Ag/a-$TiO_{2(80\,nm)}$/Ag devices.[58] It should be highlighted that IJP permits the development of layers with different thicknesses, without any supplementary fabrication process. Consequently multiple

functionalities on the same substrate, using a universal fabrication method and the same materials, are enabled.

3.1. Event-based continuous and repeatable conductance-state modulation

The present findings converge with biology, following the notion that associates intense stimulation with strong responses and longer-term changes in synaptic plasticity. To further explore the applicability of such biomimetic attributes, duty cycles above 60% were tested. In this experiment, V_{in} of 10 V was applied on the device based on the 350 nm active layer (device 3). In **Figure 4**a, α was set at 80%, and I_{out} exhibited again a stepwise increase with Δw considerably larger than the in the case of the lower duty cycle presented earlier. After 10 sets of pulses, Δw reached 174%, while after the second set of pulses, followed after a break of ≈1.57 s (Figure 4a), Δw further augmented up to ≈40 10^2%. Stronger potentiation was attained in the case of $\alpha = 90\%$, with Δw exceeding 100 10^2% during the second set of pulses (Figure 4b) and reaching compliance current after around 10 s (Figure S7, Supporting Information). Even though the stepwise current increase was observed under 80% duty cycle, with 90% duty cycle, the graduality was lost after the first set of pulses and sharp increase followed, implying hard switching. Figure 4d summarizes the synaptic modification evolution with the applied pulses of different duty cycles tested here, confirming the effect of duty cycle on the extent of potentiation along with the rise in adaptation after a number of iterations.

Device 3 characterization under V_{in} of 90% and 60 s duration revealed LTP lasting 1 h (Figure S7a, Supporting Information), a state that was reversed after 60 s of same polarity trigger application with reduced amplitude and frequency (Figure S7b, Supporting Information), returning the device to its initial state (reset process, Figure S7c, Supporting Information). Even though the results require further analysis, the findings connote an interplay of homeostatic regulation in a single unit cell.

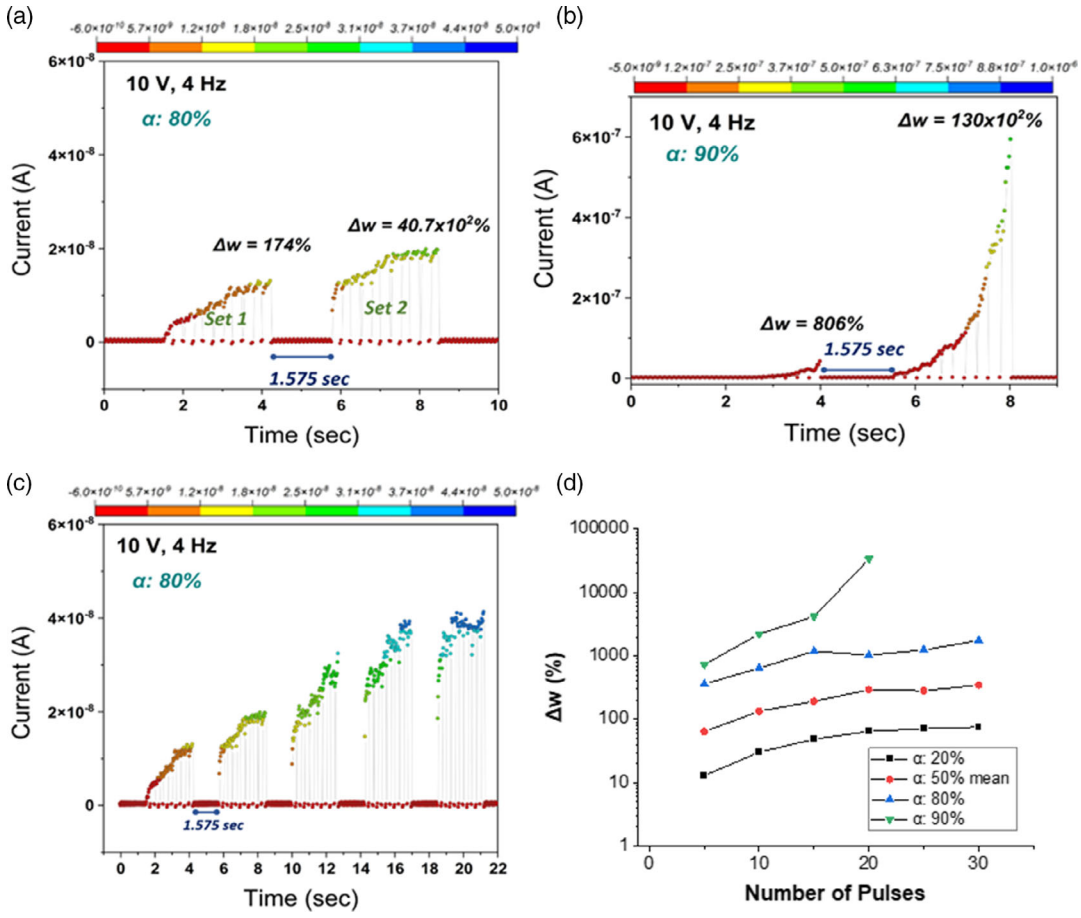

Figure 4. Effect of high duty cycle on the extend of potentiation in printed Ag/a-TiO_2/Ag electronic synapses. a) Two sets (10 pulses) of 10 V pulses with $\alpha = 80\%$ applied sequentially with 1.575 s interval on device 3 (active layer thickness: 350 nm). The Δw after the first set of pulses was 174% and after the second one Δw rose to 40.7 10^2%. In b) the α was changed to 90%, and the I_{out} exhibited a Δw of 806% and 130 × 10^2% after the first and second set of pulses, respectively, implying hard switching with abrupt current increase after 20 pulses. The follow up triggering increased the current up to compliance current (Figure S7, Supporting Information). c) The *I-t* plot under α: 80% trigger during 21 s, presenting a stepwise current increase with the applied pulses d) Δw versus number of pulses plot summary, illustrates the correlation between the extend of potentiation and the number of iterations under the various duty cycles tested on printed Ag/a-TiO_2/Ag electronic synapses, showing similar properties with an effect of habituation after 15 pulses when α was up to 80%. However, in the case of $\alpha = 90\%$, a steep current increase was induced.

Homeostatic regulation is an inherent mechanism found in neuronal systems, that keeps the synaptic activity within a useful dynamic range, by changing the synaptic efficacy Δw through sliding threshold,[64] that is, an LTP induction threshold that changes according to the timing characteristics of the preceded triggers. Homeostasis secures the long-term stability in neuronal networks,[65,66] and it is attractive as a mechanism to attain complete biomimicity with error-tolerant attributes for high-performance neural networks.

To further confirm that conductance modulation through duty cycle can be reliably achieved, a series of triggers consisting of 50 × high and 50 × low α were applied sequentially with 2 s intervals on a printed Ag/a-$TiO_{2(300\,nm)}$/Ag electronic synapse (device 3, **Figure 5**a). In the first case, the high α was set at 80% and the low at 20%. The results demonstrated an average Δw of ≈55% at α: 80% and $\Delta w \approx$ 20% at α: 20%, while in the second case, where high $\alpha = 90\%$ and low $\alpha = 10\%$, the corresponding Δw reached 100% and Δw: 27–30%, respectively. The results show that 90% duty cycle has long-term effects in conductance, which are not affected by the low duty cycle and voltage breaks mediated. However, under 80–20% duty cycles, continuous I_{out} level control is achieved with increase and decrease, respectively. Device 3 exhibited repeatable switching for more than 2×10^3 pulses (the subsequent sweeps can be found in supplementary information, Figure S8, Supporting Information). This is a significant achievement for printed electronic synapses, considering that reports on repeatability and endurance on these types of devices are scarce.

3.2. I–V Curves

In **Figure 6**, the *I–V* curves of devices based on 80 nm (Figure 6a, b**)** and 350 nm (Figure 6c,d**)** a-TiO_2 are presented. The device based on thin active layer was governed by ohmic conduction, as shown in Figure 6b, where the current increase was linear. These devices demonstrated low dynamic range (Figure 6b) and low cyclability when triggered by high duty cycle pulses (Figure S11, Supporting Information). Devices based on the 350 nm a-TiO_2 layer exhibited better dynamic range (Figure 6c,d) with repeatable characteristics for over $2\,10^3$ cycles (Figure 5, Figure S8, Supporting Information). In both cases, the first sweep demonstrated a wider loop (green lines in Figure 6a,c and dotted lines in Figure 6b,d) that is most possibly attributed to the formation of a conductive path inside the active layer. The conductive path can be single- or multiple-filament formation that relies on Ag diffusion through the active and on active layer defects.[40,67–69] Grain boundaries arose from the granular morphology of the developed a-TiO_2 layers (Figure 1d,e) which can also accommodate the build-up of conductive filaments across grain boundaries. The size and distribution of these filaments are conditional to nanograin characteristics.[70] Small ones enable the creation of multiple thin easily relocated filaments, resulting in fast current increase (Figure 5b, S10a,b, Supporting Information), susceptible to variability. However, with larger grains, thicker and stronger filaments can be shaped, leading to better dynamic range (Figure S10c,d, Supporting Information) and RS cyclability (Figure 5a, S8, Supporting Information). The grain boundaries are shown to be potential mediators for efficient RS control.[71–73] Conclusively, thin devices require optimization toward reliability, whereas thick electronic synapses are promising as neuromorphic computational nodes, owing to repeatable and durable synaptic properties.

The log–log-scale plots of device 3 are presented in Figure S10, Supporting Information, and indicate the interplay of SCLC and trapping–detrapping of charge carriers during the sweep repetition, as shown to be responsible in TiO_2-based devices.[33,34,63,74] The characterization under different frequencies also showed frequency dependence in conductance increase, suggesting frequency-encoding capabilities.

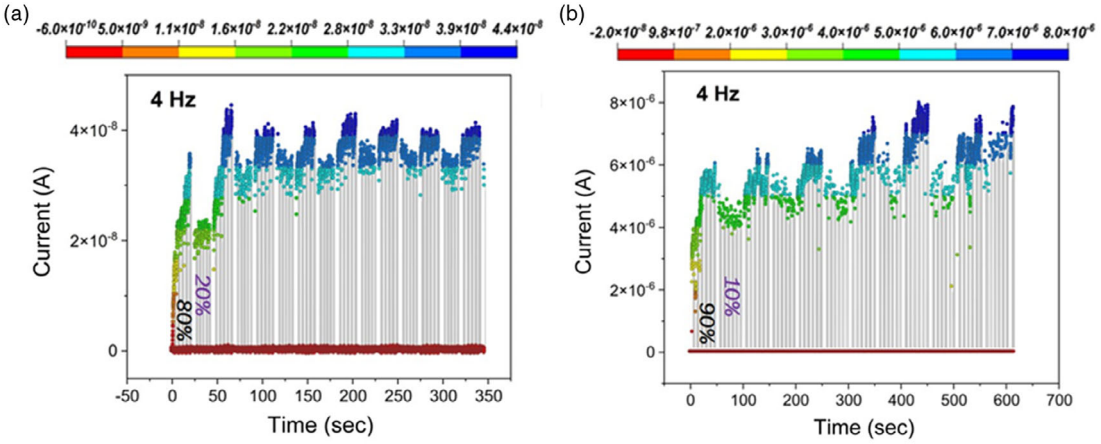

Figure 5. Sequential conductance state modulation through soft and hard stimulation, controlled by changing only pulsed triggers duty cycle. V_{in} (10 V, 4 Hz). a) 50 pulses of high (80%) and 50 of low (20%) α were applied sequentially with 2 s interval, for ≈350 s on device 3. I_{out} exhibited continuous rise and fall conditional to the duty cycle. Devices 3 demonstrated a repeatable behavior for over 2×10^3 pulses (the follow up cycles at higher frequencies can be found in Figure S8, Supporting Information). b) 50 pulses of high (90%) and 50 of low (10%) α were applied sequentially with 2 s interval, for ≈350 s on device based on 200 nm active layer thickness. I_{out} exhibited an increase independent to the mediation of lower duty cycle.

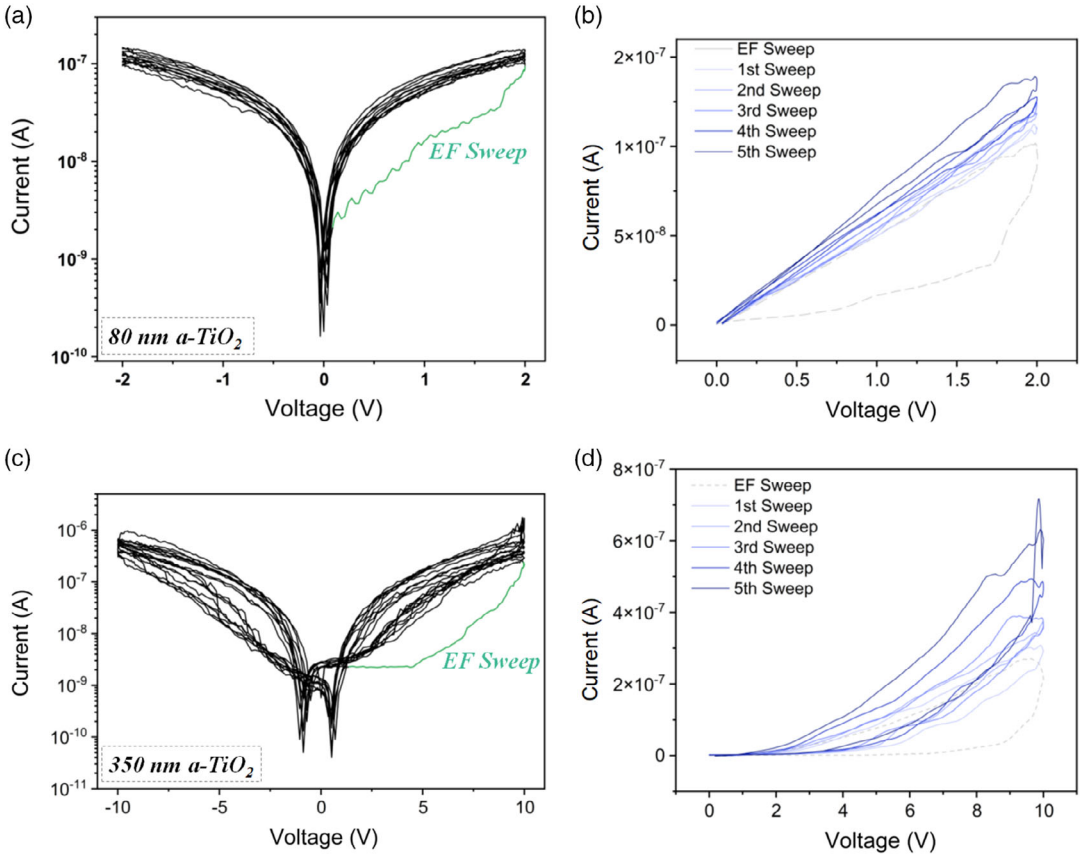

Figure 6. *I–V* plots of 80 and 350 nm a-TiO_2 - based printed synapses. a) Semilogarithmic plot of −2 to 2 V sinusoidal voltage of thin active device and the corresponding lin-lin plot for the first five sweeps shown in b), demonstrating low dynamic range compared to the 350 nm a-TiO_2 - based device. c) Semilogarithmic plot of −10 to 10 V sinusoidal voltage of the 350 nm a-TiO_2 -based device and the corresponding lin-lin plot for the first five sweeps shown in d). In both cases the initial sweep is characterized by a wider loop indicating higher resistance during the first cycle (shown in green). This effect is attributed to the electroforming process that initiates the resistive switching process in both this and thick devices.

4. Conclusion

In summary, we presented fully printed Ag/a-TiO_2/Ag electronic synapses with RS properties that emulate synaptic plasticity properties that are vital for brain-inspired processing. The formulation of custom-made inks used in this work provides a low-cost and ecofriendly alternative toward large-area and flexible neural networks. Through the versatile route of a-TiO_2 synthesis, the issues of nozzle clogging and sedimentation were effectively controlled, giving an optimal shelf life, highly encouraging for translation toward large-scale manufacturing. Furthermore, a repeatable and reliable control of a-TiO_2 thickness with nanometer-range resolution was achieved. The layer thickness was directly controlled, through the number of IJP scans, without entailing any supplementary fabrication or treatment process. The electrical characterization of the printed devices demonstrated rich internal dynamics, emulating those of Ca^{2+} that biological synapses implement for synaptic weight adjustment. We also presented that devices with thick active layers exhibited durable RS and conduction mechanism comparable with conventionally developed devices. Most importantly, the conductance state was continuously modulated via duty cycle, by implementing a single-polarity voltage trigger, therefore minimizing the power requirements while also enabling complete biomimicity when characterized under realistic operating conditions.

5. Experimental Section

Active Ink Synthesis and Characterization: a-TiO_2 nanoparticle suspension ink was developed and used for fully printed electronic synapses. The ink comprised titanium isopropoxide TTIP: Ti (IV) (97%), acetic acid (AcOH, CH_3COOH), and acetylacetone (ACAC, C5H8O2) as chelating agents. Propylene glycol methyl ether (PGME, main) and ethylene glycol ($C_2H_6O_2$) were used as solvents. First, 5 mL of a main solvent was mixed and stirred vigorously (1000 rpm with magnetic stirrer) with stabilizing agents (SA) glacial acetic acid:acetylacetone of 1:1 molar ratio, and then TTIP was added drop wise. Ink_1 had TTIP:SA molar ratio of 1:8 and Ink_2 of 1:4. Both were stirred for 3 days, under ambient conditions. Then, the solution was filtered using a 0.2 µm PTFE filter, and ethylene glycol was added (50% vol) and stirred for 1 h before its transfer to the printer cartridge.

Ink nanoparticle size was measured through DLS, using Zetasizer Nano ZSP (Malvern Instruments Ltd., UK). The viscosity and surface tension values were extracted using a Brookfield rheometer, and the surface tension was measured through a Theta (Biolin Scientific) instrument, respectively. pH measurement was carried out using the Hanna pH 213 instrument. XPS analysis was performed through

K-Alpha + spectrometer (ThermoFisher Scientific Instruments, East Grinstead, UK). The spectra were obtained through a monochromated Al Kα X-Ray source ($h\nu = 1486.6$ eV) with ≈32 mN m^{-1} and an X-Ray spot of ≈400 μm radius. Pass energy of 200 eV was used for survey spectra acquisition. Spectra were charge referenced against the C1*s* peak at 285 eV to correct for charging effects during acquisition.

Devices Fabrication, Morphology, and Electrical Characterization: All the layers that made up the electronic synapses were deposited through inkjet printing using Fujifilm Dimatix (DMP-2800 series) with a DMCLCP-11 610 cartridge (10 pL nominal droplet volume), in drop-on-demand mode and in ambient conditions. The glass substrates were cleaned with acetone, isopropanol, by 2 min argon RF plasma etching (100 W, Quorum K1050X). For bottom and top electrodes, nanosilver ink was used (Ag nanoparticle ink dispersed in ethanol, Kunshan Hisense Electronics Co., Ltd.). As active layer, the formulated custom-made TiO_2 inks were implemented. The layers were formed using a single-cartridge nozzle. For solvent evaporation and thin film formation, sintering at 120 °C for ≈20 min for electrodes and at 90 °C for 10 min for the active layer followed immediately from printing. The device active area, that is, the intersection of metal active–metal, was ≈100 μm × 100 μm for all the devices tested here. Electrode pads (600 μm × 600 μm) were deposited at 1 mm from the active area to facilitate electrical measurements and protect the device. As a last step, the active areas were encapsulated with Teflon (AF1600X, Dupont, Wilmington, DE), dissolved in[75] Fluorinert (FC-43, 3M Company, Maplewood, MN) to 1 wt%.[76]

The thickness and morphology of the developed layers were characterized through profilometry (Bruker Dektak) and microscopy cross-section SEM (Tescan FERA4 dual beam). To facilitate imaging, the layers were printed on *p*-Si substrate, after spin coating the polymer (P11) that was used as the underlayer to achieve layer uniformity. For the milling process, a Pt protective layer was deposited on top of the printed layers, and electron Pt-EBID (beam characteristics: 5 keV and 0.4 nA) and ion (Pt-IBID, beam characteristics: 30 keV and 0.3 nA) beams were used. The cross sections were done with Ga+ beam (30 keV and 0.50 nA).

For the ink characterization through TEM, drops of the developed ink solutions were placed on a copper grid coated with a carbon film and annealed at 70 °C for 2–3 min. JEOL JEM-2100F instrument and GATAN Microscopy Suite software were used for observation. The measurements were conducted at CEA Le Ripault (France).

The electrical characteristics of the printed devices were tested using Keithley 4200-SCS semiconductor parameter analyzer and Wentworth probe station. In all cases, the bottom electrode was grounded, and the top electrode was biased. Voltage amplitude was set at 1–10 V, depending on the active layer thickness (the V_{in} amplitude for each case is referred in the main text). Compliance current, used to protect the samples, was set at 10 μα for the devices 1 and 2 and 1 mA for the devices based on thicker active layers (device 3 and 4). The duty cycle was defined as $\alpha =$ pulse duration/period (%). All measurements occurred in a current-visible mode (I_{out} measurement took place simultaneously with voltage bias) and took place under ambient conditions.

Supporting Information

Supporting Information is available from the Wiley Online Library or from the author.

Acknowledgements

The authors would like to thank Dr. Steven Hinder for his support with X-Ray photoelectron spectroscopy measurements. Mr. You Matsuura and Dr. Mateus G. Masteghin are also acknowledged for their assistance with the surface tension and SEM measurements, respectively. The authors are thankful to Dr. Brice Le Borgne and GREMAN Institute and CERTEM, University of Tours (France), for the assistance with TEM characterization. This work was financially supported in part by the EPSRC (Grant ref EP/P02579X/1) and Altro Ltd.

Conflict of Interest

The authors declare no conflict of interest.

Data Availability Statement

The data that support the findings of this study are available from the corresponding author upon reasonable request.

Keywords

a-TiO_2, inkjet printed, inks, nanolayers, neuromorphic, plasticity

Received: March 28, 2022
Published online:

[1] B. Widrow, *An Adaptive "Adaline" Neuron Using Chemical "Memistors"*, California, **1960**.
[2] B. Widrow, M. E. Hoff, *Adapt. Switching Circuits* **1989**, 709.
[3] D. S. Jeong, K. M. Kim, S. Kim, B. J. Choi, C. S. Hwang, *Adv. Electron. Mater.* **2016**, *2*, 1600090.
[4] A. Citri, R. C. Malenka, *Neuropsychopharmacology* **2008**, *33*, 18.
[5] R. C. Atkinson, R. M. Shiffrin, *Human Memory: A Proposed System and its Control Processes*, Vol. *2*, Academic Press, New York, **1968**.
[6] T. Hasegawa, K. Terabe, T. Tsuruoka, M. Aono, *Adv. Mater.* **2012**, *24*, 252.
[7] N. Ilyas, D. Li, C. Li, X. Jiang, Y. Jiang, W. Li, *Nanoscale Res. Lett.* **2020**, *15*, 1.
[8] S. Li, F. Zeng, C. Chen, H. Liu, G. Tang, S. Gao, C. Song, Y. Lin, F. Pan, D. Guo, *J. Mater. Chem. C* **2013**, *1*, 5292.
[9] M. Zhao, B. Gao, J. Tang, H. Qian, H. Wu, *Appl. Phys. Rev.* **2020**, *7*, 011301.
[10] A. Mehonic, A. Sebastian, B. Rajendran, O. Simeone, E. Vasilaki, A. J. Kenyon, *Adv. Intell. Syst.* **2020**, *2*, 2000085.
[11] N. Spruston, G. Stuart, M. Häusser, *Dendrites*, Oxford University Press, **2016**, 351.
[12] S. L. Jackman, W. G. Regehr, *Neuron* **2017**, *94*, 447.
[13] R. S. Zucker, *Ann. Rev. Neusci.* **1989**, *12*, 13.
[14] B. Mockett, C. Coussens, W. C. Abraham, *Eur. J. Neurosci.* **2002**, *15*, 1819.
[15] G. L. Bliss, *Nature* **1993**, *361*, 31.
[16] G. Q. Bi, M. M. Poo, *J. Neurosci.* **1998**, *18*, 10464.
[17] H. Markram, W. Gerstner, P. J. Sjöström, *Front. Synaptic Neurosci.* **2011**, *3*, 1.
[18] P. P. Atluri, W. G. Regehr, *J. Neurosci.* **1996**, *16*, 5661.
[19] M. Graupner, N. Brunel, *Proc. Natl. Acad. Sci. U.S.A.* **2012**, *109*, 3991.
[20] W. A. Catterall, A. P. Few, *Neuron* **2008**, *59*, 882.
[21] W. Gerstner, M. Lehmann, V. Liakoni, D. Corneil, J. Brea, *Front. Neural Circuits* **2018**, *12*, 1.
[22] M. A. Erickson, L. A. Maramara, J. Lisman, *J. Cognit. Neurosci.* **2010**, *22*, 2530.
[23] S. Della Sala, *Forgetting* (Ed: S. D. Sala), Psychology Press, Sussex, **2010**.
[24] P. S. Ioannou, E. Kyriakides, O. Schneegans, J. Giapintzakis, *Sci. Rep.* **2020**, *10*, 1.
[25] E. Linn, M. Di Ventra, Y. V. Pershin, *Resist. Switching* **2016**, *1*, 31.
[26] J. J. Yang, D. B. Strukov, D. R. Stewart, *Nat. Nanotechnol.* **2013**, *8*, 13.
[27] F. C. Chiu, *Adv. Mater. Sci. Eng.* **2014**, *16*, 2014.
[28] E. W. Lim, R. Ismail, *Electronics* **2015**, *4*, 586.
[29] I. Salaoru, Q. Li, A. Khiat, T. Prodromakis, *Nanoscale Res. Lett.* **2014**, *9*, 1.

[30] E. Gale, *Semicond. Sci. Technol.* **2014**, *29*, 1.
[31] B. Prasai, B. Cai, D. A. Drabold, M. K. Underwood, A. P. Lewis, in *Mater. Sci. Technol. Conf. Exhib. 2011, MS T'11*, Vol. *1*, **2011**, p. 12.
[32] H. Zhang, B. Chen, J. F. Banfield, G. A. Waychunas, *Phys. Rev. B: Condens. Matter Mater. Phys.* **2008**, *78*, 214106.
[33] X. Cao, X. M. Li, X. D. Gao, Y. W. Zhang, X. J. Liu, Q. Wang, L. D. Chen, *Appl. Phys. A: Mater. Sci. Process.* **2009**, *97*, 883.
[34] L. Michalas, S. Stathopoulos, A. Khiat, T. Prodromakis, *Appl. Phys. Lett.* **2018**, *113*, 143503.
[35] N. Ghenzi, M. Barella, D. Rubi, C. Acha, *J. Phys. D: Appl. Phys.* **2019**, *52*, 0.
[36] F. Gul, *Ceram. Int.* **2018**, *44*, 11417.
[37] L. Zou, *Curr. Appl. Phys.* **2021**, *24*, 32.
[38] T. Fu, X. Liu, H. Gao, J. E. Ward, X. Liu, B. Yin, Z. Wang, Y. Zhuo, D. J. F. Walker, J. Joshua Yang, J. Chen, D. R. Lovley, J. Yao, *Nat. Commun.* **2020**, *11*, 1.
[39] D. V. Christensen, R. Dittmann, B. Linares-Barranco, A. Sebastian, M. Le Gallo, A. Redaelli, S. Slesazeck, T. Mikolajick, S. Spiga, S. Menzel, I. Valov, G. Milano, C. Ricciardi, S.-J. Liang, F. Miao, M. Lanza, T. J. Quill, S. T. Keene, A. Salleo, J. Grollier, D. Marković, A. Mizrahi, P. Yao, J. J. Yang, G. Indiveri, J. P. Strachan, S. Datta, E. Vianello, A. Valentian, J. Feldmann, et al., *Neuromorph. Comput. Eng.* **2022**, 1, https://doi.org/10.1088/2634-4386/ac4a83.
[40] X. B. Yan, J. H. Zhao, S. Liu, Z. Y. Zhou, Q. Liu, J. S. Chen, X. Y. Liu, *Adv. Funct. Mater.* **2018**, *28*, 1.
[41] H. Lim, H. W. Jang, D. K. Lee, I. Kim, C. S. Hwang, D. S. Jeong, *Nanoscale* **2013**, *5*, 6363.
[42] H. Y. Jeong, J. Y. Lee, S. Y. Choi, *Appl. Phys. Lett.* **2010**, *97*, 1.
[43] S. Khan, L. Lorenzelli, R. S. Dahiya, *IEEE Sens. J.* **2015**, *15*, 3164.
[44] J. Oliveira, R. Brito-Pereira, B. F. Gonçalves, I. Etxebarria, S. Lanceros-Mendez, *Org. Electron.* **2019**, *66*, 216.
[45] X. Chen, S. S. Mao, *Chem. Rev.* **2007**, *107*, 2891.
[46] Y. Jeong, M. Sim, J. H. Shin, J. W. Choi, J. I. Sohn, S. N. Cha, H. Choi, C. Moon, J. E. Jang, *RSC Adv.* **2015**, *5*, 40363.
[47] M. Coll, J. Fontcuberta, M. Althammer, M. Bibes, H. Boschker, A. Calleja, G. Cheng, M. Cuoco, R. Dittmann, B. Dkhil, I. El Baggari, M. Fanciulli, I. Fina, E. Fortunato, C. Frontera, S. Fujita, V. Garcia, S. T. B. Goennenwein, C. G. Granqvist, J. Grollier, R. Gross, A. Hagfeldt, G. Herranz, K. Hono, E. Houwman, M. Huijben, A. Kalaboukhov, D. J. Keeble, G. Koster, L. F. Kourkoutis, et al., *Appl. Surf. Sci.* **2019**, *482*, 1.
[48] S. Park, C. H. Kim, W. J. Lee, S. Sung, M. H. Yoon, *Mater. Sci. Eng. R Rep.* **2017**, *114*, 1.
[49] J. Li, F. Rossignol, J. Macdonald, *Lab Chip* **2015**, *15*, 2538.
[50] A. Lee, K. Sudau, K. H. Ahn, S. J. Lee, N. Willenbacher, *Ind. Eng. Chem. Res.* **2012**, *51*, 13195.
[51] T. Tuladhar, in *Handbook of Industrial Inkjet Printing: A Full System Approach* (Ed: W. Zapka), Wiley-VCH Verlag GmbH & Co. KGaA., Weinheim, **2017**, pp. 409–430.
[52] B. Erdem, R. A. Hunsicker, G. W. Simmons, E. David Sudol, V. L. Dimonie, M. S. El-Aasser, *Langmuir* **2001**, *17*, 2664.
[53] J. Spiridonova, A. Katerski, M. Danilson, M. Krichevskaya, M. Krunks, I. Oja Acik, *Molecules* **2019**, *24*, 4326.
[54] V. Prusakova, C. Collini, M. Nardi, R. Tatti, L. Lunelli, L. Vanzetti, L. Lorenzelli, G. Baldi, A. Chiappini, A. Chiasera, D. Ristic, R. Verucchi, M. Bortolotti, S. Dirè, *RSC Adv.* **2017**, *7*, 1654.
[55] M. J. Jackman, A. G. Thomas, C. Muryn, *J. Phys. Chem. C* **2015**, *119*, 13682.
[56] R. Koivunen, R. Bollström, P. Gane, *AIP Adv.* **2020**, *10*, 055309.
[57] B. He, S. Yang, Z. Qin, B. Wen, C. Zhang, *Sci. Rep.* **2017**, *7*, 1.
[58] B. Salonikidou, T. Yasunori, B. Le Borgne, J. England, T. Shizuo, R. A. Sporea, *ACS Appl. Electron. Mater.* **2019**, *1*, 2692.
[59] L. L. Hench, R. Orefice, *Kirk-Othmer Encyclopedia of Chemical Technology*, John Wiley & Sons, Inc., Hoboken, NJ, **2000**.
[60] F. Zenke, G. Hennequin, W. Gerstner, *PLoS Comput. Biol.* **2013**, *9*, e1003330.
[61] J. Fiser, P. Berkes, G. Orbán, M. Lengyel, *Trends Cognit. Sci.* **2010**, *14*, 119.
[62] M. Prezioso, F. Merrikh Bayat, B. Hoskins, K. Likharev, D. Strukov, *Sci. Rep.* **2016**, *6*, 2.
[63] B. Roux, *Neuron* **2006**, *52*, 568.
[64] M. H. Lee, K. M. Kim, G. H. Kim, J. Y. Seok, S. J. Song, J. H. Yoon, C. S. Hwang, *Appl. Phys. Lett.* **2010**, *96*, 219901.
[65] H. K. Lee, A. Kirkwood, *Front. Cell. Neurosci.* **2019**, *13*, 1.
[66] R. Narayanan, D. Johnston, *J. Neurophysiol.* **2010**, *104*, 1020.
[67] S. Kim, C. Du, P. Sheridan, W. Ma, S. Choi, W. D. Lu, *Nano Lett.* **2015**, *15*, 2203.
[68] T. Tsuruoka, T. Hasegawa, K. Terabe, M. Aono, *Nanotechnology* **2012**, *23*, 435705.
[69] X. Zhu, C. Du, Y. Jeong, W. D. Lu, *Nanoscale* **2017**, *9*, 45.
[70] E. Verrelli, D. Tsoukalas, *Solid. State. Electron.* **2014**, *101*, 95.
[71] D. S. Jeong, H. Schroeder, U. Breuer, R. Waser, *J. Appl. Phys.* **2008**, *104*, 123716.
[72] R. Waser, R. Dittmann, M. Salinga, M. Wuttig, *Solid. State. Electron.* **2010**, *54*, 830.
[73] M. Lanza, K. Zhang, M. Porti, M. Nafra, Z. Y. Shen, L. F. Liu, J. F. Kang, D. Gilmer, G. Bersuker, *Appl. Phys. Lett.* **2012**, *100*, 123508.
[74] M. H. Lee, K. M. Kim, G. H. Kim, J. Y. Seok, S. J. Song, J. H. Yoon, C. S. Hwang, *Appl. Phys. Lett.* **2010**, *96*, 152909.
[75] T. Shi, R. Wang, Z. Wu, Y. Sun, J. An, Q. Liu, *Small Struct.* **2021**, *2*, 2000109.
[76] Y. Takeda, T. Sekine, R. Shiwaku, T. Murase, H. Matsui, D. Kumaki, S. Tokito, *Appl. Sci.* **2018**, *8*, 1331.